

# A first detailed study of the quantum decoherence of entangled gamma photons

Julien Bordes, James R. Brown, Daniel P. Watts, Mikhail Bashkanov, Ruth Newton, and Nicholas Zachariou  
*School of Physics, Engineering and Technology, University of York, York, YO10 5DD, UK.*

(Dated: December 11, 2023)

Constraints on the quantum decoherence of entangled  $\gamma$  quanta at the MeV scale, such as those produced following positron annihilation, have remained elusive for many decades. We present the first accurate, large acceptance experimental data for triple Compton scattering (TCS) of such entangled  $\gamma$ . An entanglement witness, the enhancement ( $R$ ) of the azimuthal correlation between the final CS planes, is obtained where one of the  $\gamma$  underwent intermediate Compton scattering (CS).  $R$  is found to exceed the classical limit for scatter angles up to  $\sim 40^\circ$ . The extracted  $R$ , over the range of the data ( $0 - 70^\circ$ ), are better described by simple models in which entanglement is conserved or decohered proportional to the visibility of the scatter process. The work will help guide the development of a first theoretical description of decoherence at the MeV scale, a crucial next step for fundamental physics and entangled PET medical imaging.

## I. INTRODUCTION

The quantum entanglement (QE) of photonic systems in the optical or near-optical regime (eV energy scale) underpins recent advances in quantum information, computing, encryption and teleportation [1] and are the basis of key fundamental tests of QE [2]. The decoherence of propagating entangled optical photons, due to the continuous monitoring of the state by the environment, is well studied theoretically and experimentally [3–10]. However, at the MeV scale, such as for the entangled quanta from positron annihilation, the photons interact via different interaction processes. Our knowledge of decoherence is so poor that even the role of the leading process (Compton scattering) for entangled  $\gamma$  is not understood.

Addressing this is crucial for fundamental tests of QE in new regimes of energy, for unexplored multi-partite entangled systems [11] and societal applications, such as PET imaging [12]. Entangled MeV quanta have very different properties than optical. Detection is essentially noise free, they are more penetrating through matter (enabling deeper imaging), have wavelengths  $\sim 10^6$  smaller and typically small (ns) wavepacket sizes.

The simplest source of entangled  $\gamma$  quanta is positron annihilation, i.e.  $e^+e^- \rightarrow 2\gamma$  (although entangled  $\gamma$ -quanta are in principle producible from many nuclear systems). The two  $\gamma$  are predicted to be in an entangled Bell state of linear polarization [13]. Information on linear polarization can be obtained via the Compton scattering (CS) process  $\gamma + e^- \rightarrow \gamma' + e^-$ , in which the azimuthal scatter plane ( $\phi$ ) is modulated with a  $\cos^2\phi$  amplitude relative to the incident polarization [14, 15]. For double CS (DCS), in which both  $\gamma$  undergo CS, the QE manifests as an enhanced correlation between the azimuths ( $\Delta\phi$ ) of the two CS planes, as shown independently by Snyder and Pryce and Ward [16, 17].

A correlation amplitude above the classical limit (i.e. larger than that expected from DCS of separable orthogonally polarised  $\gamma$ ) provides a witness of QE [13]. Correlations larger than the classical limit have been observed in experiments since the 1950's, typically exploiting large NaI  $\gamma$  detectors [18–25], and agree with QE theory with

analytical account experimental aspects.

DCS QE effects have recently been implemented into the leading particle transport simulation framework – Geant4 [26, 27], referred to as QE-Geant4 [12]. QE-Geant4 (QEG4) improves the description of the propagation of entangled  $\gamma$  through matter and enables more accurate modelling of acceptances and background processes. It helped establish that modern segmented  $\gamma$ -detector systems can access QE information with systems commensurate with those employed/planned for PET/SPECT medical scanners (e.g. CZT [12]). Here we adopt material and pixel sizes matching next generation EXPLORER total-body PET (also see [28–30]).

Due to the current gap in our knowledge of fundamental decoherence processes at the MeV scale, a complete loss of entanglement after the first DCS is currently assumed in QEG4 [12]. The leading process by which entangled MeV  $\gamma$  quanta from positron annihilation interact with their environment is CS. Quantifying the effect of CS on entanglement requires a measurement of triple CS (TCS), in which one of the  $\gamma$  undergoes an intermediate CS (ICS) before the azimuthal correlation ( $\Delta\phi$ ) is measured. The challenge of TCS measurement is finally being met, over 70 years after the first DCS experiments. TCS measurements, albeit with large bins of ICS polar angle, have recently been achieved [30–32].

In this work, we present a first precise measurement of azimuthal CS correlations in TCS in narrow bins of ICS angle covering  $0-70^\circ$ . The classical limit in the apparatus is established through QEG4 simulation assuming complete quantum decoherence following the first DCS. Additionally, the data are compared to QEG4 adaptations using basic models where QE is maintained or decohered according to ICS visibility.

## II. THEORETICAL BACKGROUND

The annihilation  $\gamma$  produced from the para-positronium ground state are in an entangled Bell state of linear polarization:

## QEG4-FD - Full decoherence by TCS

$$|\Psi\rangle = \frac{1}{\sqrt{2}} \left( |x\rangle_- |y\rangle_+ - |y\rangle_- |x\rangle_+ \right), \quad (1)$$

where  $|x\rangle_-$  and  $|y\rangle_-$  ( $|x\rangle_+$  and  $|y\rangle_+$ ) represent  $\gamma$  with perpendicular polarizations in  $x$  and  $y$  propagating along  $-z$  ( $+z$ ). This Bell state is the only allowed state following ground state positronium annihilation to two  $\gamma$  [13, 16, 33]. The predictions for the DCS cross section of such Bell state  $\gamma$  [17] were recently confirmed in matrix [34] and Kraus operator formalisms [35].

The cross section for DCS of the entangled (511 keV) annihilation  $\gamma$  in the Bell state, Eqn. (1), is given in [16, 17, 33] and is the basis of the QEG4 simulation for DCS (see [12]). In extending this QEG4 simulation for TCS, we adopt models based on extreme theoretical ansatz. One establishes the classical limit (QEG4-FD) and one approximates TCS where entanglement is fully maintained (QEG4-ENT). In their discussion we use the nomenclature convention ( $\gamma_{1,1',2,2'}$ ) in Fig. 1.

$$\frac{d^2\sigma}{d\Omega_1 d\Omega_{2'}} = \frac{k_1^2 k_2'^2 (\alpha_1 \alpha_{2'} - \alpha_1 \sin^2(\theta_{2'}) - \alpha_{2'} \sin^2(\theta_1) + 2 \sin^2(\theta_1) \sin^2(\theta_{2'}) \sin^2(\Delta\phi)}{4\pi^2 k_1^2 \left(\frac{40}{9} - 3 \ln(3)\right)^2} \quad (2)$$

where  $\alpha_1 = \frac{k_{1'}}{k_1} + \frac{k_1}{k_{1'}}$  and  $\alpha_{2'} = \frac{k_{2''}}{k_{2'}} + \frac{k_{2'}}{k_{2''}}$  where  $k_1$  and  $k_{2''}$  are the momenta of  $\gamma_{1'}$  and  $\gamma_{2''}$ . For 511 keV photons, this equation reproduces the result from perturbation theory [16].

The DCS cross section (Eqn. 2) is calculated for back-to-back photons. As in TCS  $\gamma_2'$  is no longer back-to-back with  $\gamma_1$ , the  $\phi$  correlations are sampled taking  $\hat{z}$  in the direction of  $\gamma_2'$  and  $\phi$  relative to its polarization  $\hat{\epsilon}_{\gamma_2'}$  (which fixes the orientation of  $\hat{x}$ ,  $\hat{y}$ ). The orientation of  $\hat{\epsilon}_{\gamma_2'}$  is obtained from transforming  $\hat{\epsilon}_{\gamma_2}$  into the frame of  $\gamma_2'$  without rotation [39]. Subsequent processes are simulated as separable  $\gamma$ .

QEG4-ENT approximates TCS where entanglement is maintained. A decoherence postulate is that the initial Bell state evolves a separable component with probability proportional to the ( $\theta_{ICS}$  dependent) ‘‘visibility’’ to linear polarization in the ICS process, which is [40]. The QEG4-ENT(Vis) simulation additionally includes this decoherence postulate.

This model provides the classical limit (CL) for azimuthal correlations in TCS from an initially entangled  $\gamma$ - pair ( $\gamma_{1,2}$ ) undergoing DCS and produces two independent (separable) photon states ( $\gamma_{1',2'}$ ). QEG4-FD is the current TCS modelling in QEG4 [36]. (See [37] if simulating TCS with the current development version (11.1) of QEG4.)

## QEG4-ENT - A basic model for entangled TCS

No theoretical prediction of the TCS cross section for annihilation- $\gamma$  is currently available. We therefore adopt a simple model to approximate the azimuthal correlations between  $\gamma_1$  and  $\gamma_2'$  where the initial entanglement (between  $\gamma_1$  and  $\gamma_2$ ) is maintained between  $\gamma_1$  and  $\gamma_2'$ , with the ICS only reducing the energy of  $\gamma_2'$ . The DCS of  $\gamma_1$  and  $\gamma_2'$  are therefore as expected from a Bell state. Predictions are obtained from the formalism of Snyder, Pasternack and Hornbostel (SPH) [16] (Eqn. 2), derived using a ‘‘partial polarization’’ ansatz in which the CS (modelled by standard Klein-Nishina (KN) theory) is factored from the Bell state [38]. The DCS cross section in SPH formalism (using our  $\gamma$  nomenclature for TCS) is given by:

### A. Experimental apparatus

A Geant4 visualisation of our apparatus is shown in Fig.1. Two segmented detector modules (DM) each comprising 256 3x3x20 mm<sup>3</sup> LYSO scintillator crystals coupled to arrays of Ketek PM3325-WB-D0 silicon photomultipliers (SiPMs) were positioned either side of a  $\sim 1.8$  MBq <sup>22</sup>Na source, with centres 48 mm from the source. An additional 3x3x5 mm<sup>3</sup> LYSO *scatter* detector (SCD) was placed between the source and DM0, with centre 6.8 mm from the source and longest side oriented vertically. Data acquisition employed Peltier cooled PETsys-TOFPET2 ASICs [41]. The CS polar angle in the SCD ( $\theta_{ICS}$ ) was calculated from the deposited energy. A separate data set was also obtained with DM0 rotated 28° about the source position.

A typical TCS event is shown (green lines) comprising a hit in the SCD coincident with double-hit CS candidates in DM0/DM1. The experimental trigger was a 15 ns coincidence between SCD and DM0/1 ( $\pm 2$  ns achieved in offline analysis). Calibration using reference laboratory sources and intrinsic radioactivity provided six points (31.4–1274.5 keV) fitted by 4<sup>th</sup> order poly-

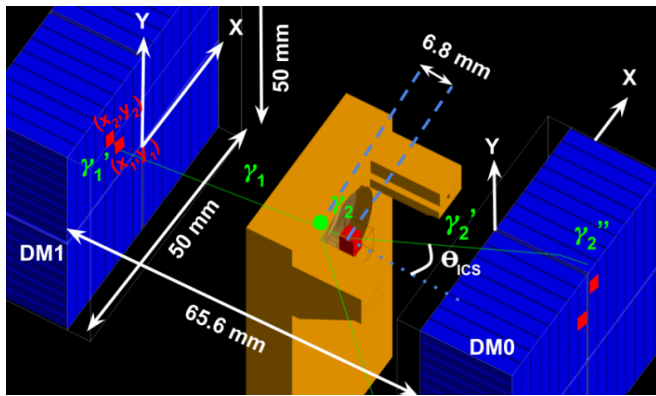


FIG. 1. G4 visualisation showing source location (green circle), holder (orange), SCD (red cube), LYSO pixels of the DM0/DM1 detectors (blue). Detector windows/enclosures shown by white lines, PCBs omitted for clarity. Green lines show particle tracks from a single TCS event. The  $\gamma$  referencing ( $\gamma_{1,1',1'',2,2',2''}$ ), is identified next to the tracks. Red pixels show the energy deposits in DM0/1.

mial. For SCD,  $\gamma$ 's at 59.54 and 122.06 keV were additionally used. The SCD noise threshold was  $\sim 7$  keV and energy resolution 12.2% FWHM. Gain drifts in SCD and DM0/1 ( $\sim 5\%$ ) were corrected using the 511 keV photopeak. The energy resolution for summed double hits (SDH) was 12.4% (14.3%) FWHM at 511 keV for DM0 (DM1).

The full apparatus, including wrappings, reflectors, PCBs, circuit boards, detector housings and source was reproduced in the QEG4 simulation. Predicted energy deposits were smeared according to the resolutions above. SDH peak centroids in data and simulation agreed within  $\sim 2\%$  [42].

### B. Analysis methods

The experimental data and the QEG4 pseudo-data were passed through the same analysis code. The CS polar angle in each head were calculated from the larger of the two energy deposits using CS kinematics. For discussion see [12].

The  $\phi$  were calculated using the location of the two pixel-hits in each DM array,  $x_{1,2}$  and  $y_{1,2}$  (Fig. 1) with  $\phi = \text{atan}\left(\frac{y_2 - y_1}{x_2 - x_1}\right)$  and resolution  $\sim 1.5^\circ - 12^\circ$  dependent on pixel separation (adjacent pixel hits were excluded). The relative azimuthal scattering angle is  $\Delta\phi = \phi_1 - \phi_2'$ . The  $\Delta\phi$  correlation amplitude is extracted using the function  $\text{Acos}(2\Delta\phi) + B$ . The enhancement ( $R$ ), the ratio of counts between  $\Delta\phi = 90^\circ$  to  $0^\circ$ , was  $R = (B - A)/(B + A)$ .

The effect of detector acceptance was corrected using event-mixing methods [43] but this produced negligible ( $\leq 2\%$ ) influence on the  $\Delta\phi$  distributions or  $R$ .

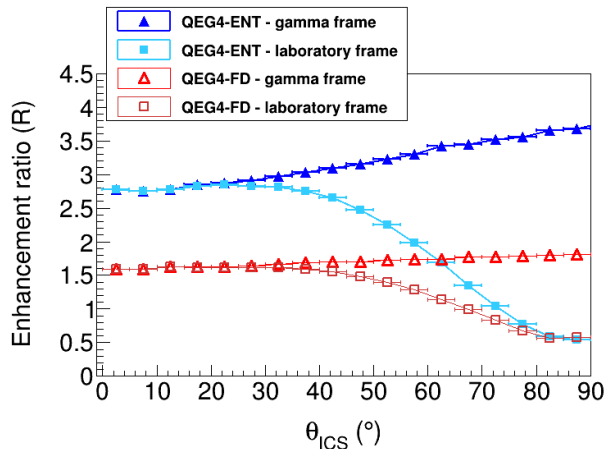


FIG. 2.  $R$  extracted from a “perfect detector” (see text) for  $\theta_{1,2'} \in 80^\circ - 84^\circ$ . Red data points show  $R$  extracted from QEG4-FD in the laboratory frame (open triangles) and photon frame (open boxes). Corresponding predictions for QEG4-ENT are shown by blue solid markers.

### III. RESULTS

Before presenting the QEG4-ENT and QEG4-FD models within the detector acceptance it is informative to obtain predictions for a “perfect” detector. This was a (simulated) isotropic water sphere, with the source at its centre, and using exact hit information for pure TCS events. The extracted  $R$  for  $\theta_{1,2'} \in 80^\circ - 84^\circ$  are shown (Fig 2) for two measurement frames. For QEG4-FD the red square markers show the  $R$  extracted in the fixed laboratory frame. For  $\theta_{ICS} \rightarrow 0^\circ$ ,  $R$  converges near to the expected value ( $R = 1.63$ ) for a separable state [13] in DCS[44].

The red triangular data points show the QEG4-FD  $R$  values extracted in the photon frame, where the  $\phi$  angle of  $\gamma_2'$  is determined with respect to the polarization of  $\gamma_2'$  (known for each simulated event). In this frame  $R$  rises with  $\theta_{ICS}$ , reflecting increasing CS analysing power as the  $\gamma$  energy reduces. The QEG4-ENT model (blue data points) shows the (expected) [13]  $R$  value of  $\sim 2.7$  at small  $\theta_{ICS}$ . For larger  $\theta_{ICS}$ , similar general features as QEG4-FD are evident between the two frames.

Examples of the experimental  $\Delta\phi$  distributions and  $R$  fits (in the laboratory frame) for different  $\theta_{ICS}$  bins are shown in Fig. 3. Systematic errors in  $R$  are  $\sim 5\%$  [45]. The extracted  $R$  are presented as a function of  $\theta_{ICS}$  in Fig. 4 with black (red) data points for back-to-back (DM0 rotated through  $28^\circ$ ) datasets. The two datasets are consistent to  $\leq 8\%$  where they overlap. The datum at  $\theta_{ICS} = 0^\circ$  is obtained without SCD but with DM1 acceptance cuts to match the hit distribution for SCD coincidence events. Below  $\theta_{ICS} \sim 35^\circ$   $R$  shows a modest decrease of  $\sim 6\%$  with increasing CS angle. For larger angles,  $R$  diminishes more rapidly until around  $70^\circ$ , approaching  $R=1$ .

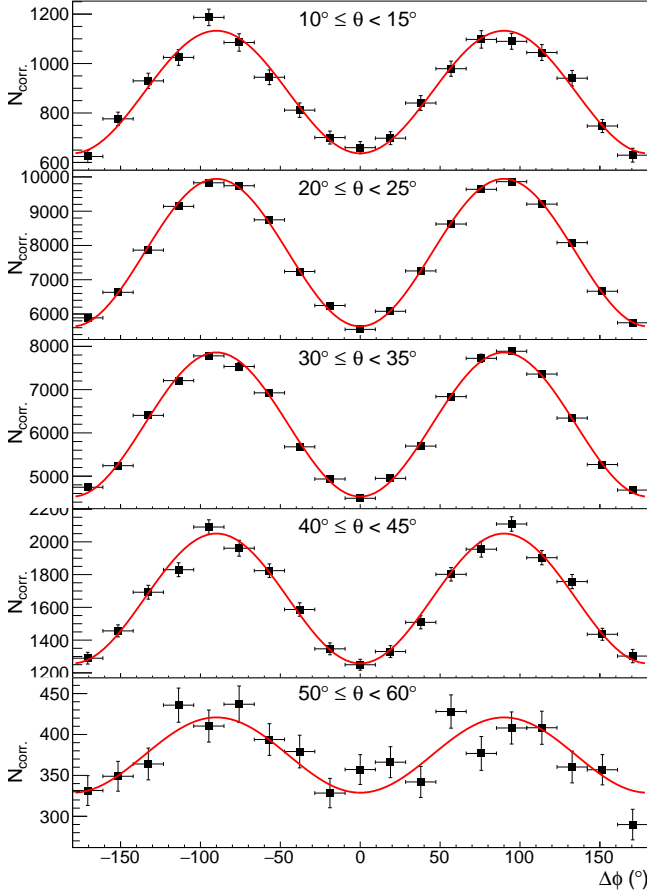


FIG. 3. Measured  $\Delta\phi$  distributions for events with  $\theta_{1,2'} \in 72^\circ - 92^\circ$  for a range of  $\theta_{ICS}$  bins (indicated above each panel). Red lines show the fits to extract  $R$ .

All previous TCS data [12, 30–32] are consistent with the current data within their larger bins and statistical accuracy (since the measured  $R$  is apparatus dependent, the other datasets are normalised according to the current  $R$  at  $\theta_{ICS} \sim 0^\circ$ ).

The predictions from the QEG4-FD model for all events in the detector acceptance, which provides the classical limit, are shown by the purple band - QEG4-FD(all). The experimental data exceed this limit up to  $\theta_{ICS} \sim 45^\circ$ , witnessing significant levels of entanglement even with an ICS. To assess the fidelity of the classical limit we also show predictions where the  $\gamma$  *only* underwent TCS - QEG4-FD(TCS). The agreement between QEG4-FD(all) and QEG4-FD(TCS) shows the classical limit is defined with little ambiguity, apart from at large  $\theta_{ICS}$ . In this region, contributions from unresolved multiple scattering processes within detector pixels, increasingly compete with the (diminished) cross section for large angle CS. We note that such multiple scattering of separable  $\gamma$  are appropriately modelled by the standard KN classes.

The predictions of the QEG4-ENT model for all events

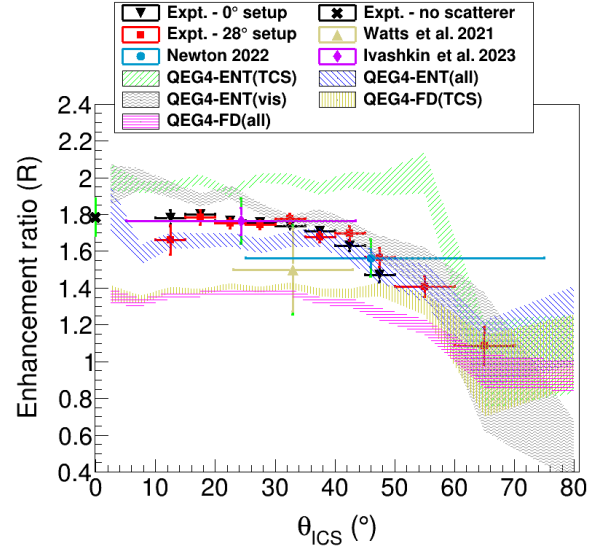


FIG. 4.  $R$ , versus  $(\theta_{ICS})$  for  $\theta_{1,2'} \in 72^\circ - 92^\circ$ . Red (black) data points for back-to-back (rotated) detector configurations. Datum at  $\theta_{ICS}=0$  (cross) is from a back-to-back apparatus without SCD (green bar shows systematic error). Beige, blue, purple data points show previous data from CZT [12], prototype LYSO [30] and NaI [32]. Purple (blue) curves show QEG4-FD (QEG4-ENT) predictions for all events in the detector acceptance. Yellow (green) bands show corresponding predictions selecting pure TCS. Grey band shows QEG4-ENT(Vis).

in the detector acceptance, QEG4-ENT(all), are shown by the blue band. This model produces a better description of the general features of the data, albeit underpredicting  $R$  at small  $\theta_{ICS}$  by up to 10% and predicting a flatter dependence. For  $\theta_{ICS} \gtrsim 40^\circ$  it predicts a less rapid diminishing of  $R$ , overpredicting the experimental data. The predictions for pure TCS, QEG4-ENT(TCS), are shown by the green band.  $R$  is increased by  $\sim 25\%$  for small  $\theta_{ICS}$  and shows a sharper fall at larger angles. The enhanced sensitivity to beyond TCS is likely exacerbated by the current model limitations. Entanglement is propagated to TCS, but subsequently the  $\gamma$  interact as separable photons ( $R$  values closer to QEG4-FD). The underprediction of the data by QEG4-ENT(all) may arise if beyond TCS processes retain some entanglement, rather than the complete loss assumed in the model.

The discrepancies between the  $\theta_{ICS}$  dependence of the data and the QEG4-ENT model (viz. the slope in the data at small  $\theta_{ICS}$  and the more rapid fall off at large angles) may provide some initial constraints on decoherence. It is interesting that the “visibility” decoherence ansatz - QEG4-ENT(Vis) (grey band) produces similar features, but with the caveat that firm interpretation requires a proper quantum theory for TCS in QEG4.

#### IV. CONCLUSION

The most fundamental reaction to constrain entanglement decoherence at the MeV scale, triple Compton scattering (TCS) has previously escaped detailed experimental scrutiny. We present the first precise and large acceptance measurements for TCS of entangled positron annihilation  $\gamma$ , covering intermediate CS angles,  $\theta_{ICS}$ , from  $0^\circ$  to  $70^\circ$ .

The enhancement ( $R$ ) between the final CS planes (an entanglement witness) is obtained as a function of  $\theta_{ICS}$ . The experimental data exceed the classical limit of  $R$  by up to  $\sim 60\%$  for  $\theta_{ICS} \lesssim 40^\circ$ , indicating significant entanglement is maintained after CS of entangled  $\gamma$ . For larger  $\theta_{ICS}$   $R$  diminishes and is comparable to the (apparatus dependent) classical limit at around  $60^\circ$ . A simple model, where the final CS planes in TCS are as expected following double CS of Bell state  $\gamma$  gives a broad, though not detailed, agreement with the experimental data. The description is improved if Bell state decoherence proportional to the ( $\theta_{ICS}$  dependent) visibility is included. Future detailed quantum theory for TCS, informed by the

current work, is a crucial next step.

As suggested in [12], the sensitivity to scatter backgrounds in QE-PET should be re-assessed now quality TCS data has been obtained (the sensitivity to random backgrounds is unaffected).

Further progress and a deeper interpretation of the data will require a proper quantum theory for TCS. Such efforts are ongoing within our group.

#### ACKNOWLEDGMENTS

We thank D. Jenkins for useful comments and insights and K. See for undergraduate project work contributing to the project. The simulation work was undertaken on the Viking Cluster, a high performance computing facility provided by the University of York. We are grateful for computational support from the University of York High Performance Computing service, Viking and the Research Computing team. The authors gratefully acknowledge the support of the UK Science and Technologies Funding Council (STFC) grant number ST/W006383/1.

- 
- [1] S. Slussarenko and G. J. Pryde, Applied Physics Reviews **6**, 041303 (2019).
  - [2] W. Tittel and G. Weihs, arXiv e-prints (2001).
  - [3] M. Schlosshauer, Physics Reports **831**, 1 (2019), quantum decoherence.
  - [4] W. H. Zurek, Physical review D **24**, 1516 (1981).
  - [5] W. H. Zurek, Physical review D **26**, 1862 (1982).
  - [6] J. P. Paz and W. H. Zurek, in *Fundamentals of quantum information: quantum computation, communication, decoherence and all that* (Springer, 2002) pp. 77–148.
  - [7] W. H. Zurek, Reviews of modern physics **75**, 715 (2003).
  - [8] M. Schlosshauer, Reviews of Modern physics **76**, 1267 (2005).
  - [9] G. Bacciagaluppi, in *The Stanford Encyclopedia of Philosophy*, edited by E. N. Zalta (Metaphysics Research Lab, Stanford University, 2020) Fall 2020 ed.
  - [10] E. Joos, H. D. Zeh, C. Kiefer, D. J. Giulini, J. Kupsch, and I.-O. Stamatescu, *Decoherence and the appearance of a classical world in quantum theory* (Springer Science & Business Media, 2013).
  - [11] B. C. Hiesmayr and P. Moskal, Scientific Reports **7** (2017), 10.1038/s41598-017-15356-y.
  - [12] D. P. Watts, J. Bordes, J. R. Brown, A. Cherlin, R. Newton, J. Allison, M. Bashkanov, N. Efthimiou, and N. A. Zachariou, Nat. Commun. , 1 (2021), arXiv:2012.04939.
  - [13] D. Bohm and Y. Aharonov, Phys. Rev. **108**, 1070 (1957).
  - [14] O. Klein and T. Nishina, Zeitschrift fur Physik **52**, 853 (1929).
  - [15] G. Eksping, *The Oskar Klein Memorial Lectures. Vol. 2: Lectures by Hans A. Bethe and Alan H. Guth, with translated reprints by Oskar Klein.* (1994).
  - [16] H. S. Snyder, S. Pasternack, and J. Hornbostel, Phys. Rev. **73**, 440 (1948).
  - [17] M. H. L. Pryce and J. C. Ward, Nature **160**, 435 (1947).
  - [18] C. S. Wu and I. Shaknov, Phys. Rev. **77**, 136 (1950).
  - [19] H. Langhoff, Zeitschrift fur Physik **160**, 186 (1960).
  - [20] L. R. Kasday, in *Foundations of Quantum Mechanics: Proceedings of the International School of Physics "Enrico Fermi"*, edited by B. d'Espagnat (Academic P XIV, 1971, 1971) pp. 195–210.
  - [21] G. Faraci, D. Gutkowski, S. Notarrigo, and A. R. Pennisi, Lettere al Nuovo Cimento (1971-1985) **9**, 607 (1974).
  - [22] L. R. Kasday, J. D. Ullman, and C. S. Wu, Il Nuovo Cimento B **25 B**, 633 (1975).
  - [23] A. Wilson, J. Lowe, and D. Butt, J. Phys. G: Nucl. Phys. **2**, 613 (1976).
  - [24] M. Bruno, M. D'Agostino, and C. Maroni, Il Nuovo Cimento B **40**, 143 (1976).
  - [25] G. Bertolini, E. Diana, and A. Scotti, Il Nuovo Cimento B **63**, 651 (1981).
  - [26] S. Agostinelli *et al.*, Nucl. Instrum. Methods in Phys. Res. A **506**, 250 (2003).
  - [27] J. Allison *et al.*, Nucl. Instrum. Methods in Phys. Res. A **835**, 186 (2016).
  - [28] M. Makek, D. Bosnar, and L. Pavelić, Condensed Matter **4**, 24 (2019).
  - [29] M. Makek, D. Bosnar, L. Pavelić, P. Šenjug, and P. Žugec, Nuclear Instruments and Methods in Physics Research, Section A: Accelerators, Spectrometers, Detectors and Associated Equipment **958**, 162835 (2020).
  - [30] R. N. Newton, PhD. thesis, University of York, UK (2022).
  - [31] D. Abdurashitov, A. Baranov, D. Borisenko, F. Guber, A. Ivashkin, S. Morozov, S. Musin, A. Strizhak, I. Tkachev, V. Volkov, and B. Zhuikov, Journal of Instrumentation **17**, P03010 (2022).
  - [32] A. Ivashkin, D. Abdurashitov, A. Baranov, F. Guber, S. Morozov, S. Musin, A. Strizhak, and I. Tkachev, Sci-

- entific Reports **13**, 7559 (2023), arXiv:2210.07623.
- [33] J. C. Ward, Ph.D. thesis, University of Oxford (1949).
- [34] P. Caradonna, D. Reutens, T. Takahashi, S. Takeda, and V. Vegh, Journal of Physics Communications **3** (2019), 10.1088/2399-6528/ab45db, arXiv:1910.05537.
- [35] B. C. Hiesmayr and P. Moskal, Scientific Reports **9**, 1 (2019), arXiv:1807.04934.
- [36] QEG4-FD is consistent with standard Geant4 ( $\gamma_{1,2}$  separable) to  $\leq 5\%$  over data range.
- [37] The current development version of QEG4 (v11.1) requires a filter on event ordering such that the polarization vectors are correctly assigned for all events.
- [38] Approach is supported by [11], where CS visibility is factored from the DCS cross section.
- [39]  $\hat{\epsilon}_{\gamma'_2}$  lies in the plane formed by the polarization of the incoming  $\gamma$ ,  $\hat{\epsilon}_{\gamma_2}$  and  $\hat{\gamma}'_2$  and is perpendicular to  $\hat{\gamma}'_2$ .
- [40] Derived from the difference in CS cross sections for orthogonally polarised 511 keV  $\gamma$  from polarised KN formula:  $V_{CS} = \frac{\sin^2(\theta)}{\frac{1}{2-\cos(\theta)} + \sin^2(\theta) - \cos(\theta)}$ .
- [41] A. Di Francesco, R. Bugalho, L. Oliveira, L. Pacher, A. Rivetti, M. Rolo, J. C. Silva, R. Silva, and J. Varela, Journal of Instrumentation **11** (2016), 10.1088/1748-0221/11/03/C03042.
- [42] Small difference attributable to light collection for crystal entry points of CS  $\gamma$  c.f. calibration data and nonlinearities in energy calibration.
- [43] The acceptance correction is:  $N_{corr}(\theta, \Delta\phi) = \frac{N_{real}(\theta, \Delta\phi)}{N_{mixed}(\theta, \Delta\phi)} \cdot \sum_{\theta, \Delta\phi=-\pi}^{\pi} N_{mixed}(\theta, \Delta\phi)$  where  $N_{real}(\theta, \Delta\phi)$  is the number of real coincident events within a given  $\theta$  and  $\Delta\phi$  bin, and  $N_{mixed}(\theta, \Delta\phi)$  is the number of mixed events for the corresponding bin.
- [44] For  $\theta_{1',2'}=81.7^\circ$   $R = 1.63$  from [13]. Current data for  $81.7^\circ \pm 2^\circ$ .
- [45] Estimated from  $R$  using  $\pm\Delta\phi$  (1.4%), 2% variation of DM0/1/SCD energy calibrations (2%), uncertainties in DM0/1 in-array crystal locations (1%), DM0/1/SCD locations (2%).